The role of diabatic heating/cooling in outer rainbands in the secondary eyewall formation and evolution in a numerically simulated tropical cyclone

Hui Wang[a], and Yuqing Wang[b]

[a]*State Key Laboratory of Severe Weather, Chinese Academy of Meteorological Sciences, Beijing, China*

[b]*International Pacific Research Center and Department of Atmospheric Sciences, University of Hawaii at Manoa, Honolulu, Hawaii*

July 2, 2024 (submitted)
September 14, 2024 (first revision)
October 8, 2024 (second revision)

Key points:

1. Increasing diabatic heating in outer rainbands leads to earlier SEF, and faster weakening and earlier dissipation of the primary eyewall.
2. Increasing diabatic cooling in outer rainbands suppresses convective activity in outer rainbands and is unfavorable for the SEF.
3. When the area-averaged diabatic heating rate in outer rainbands and the eyewall become similar in magnitude, the secondary eyewall forms.

Submitted to ***Atmospheric Research***

*Corresponding author:
Prof. Yuqing Wang
International Pacific Research Center
University of Hawaii at Manoa
404A/POST, 1680 East West Road,
Honolulu, HI 96822, USA.
Email: yuqing@hawaii.edu

Abstract

In this study, the role of diabatic heating/cooling in outer rainbands (ORBs) in the formation and evolution of the secondary eyewall of a numerically simulated tropical cyclone (TC) is investigated. This is done through a series of sensitivity experiments under idealized conditions using a high-resolution cloud-resolving atmospheric model. The results show that artificially increasing diabatic heating in rainbands enhances convective activities in ORBs and leads to an earlier secondary eyewall formation (SEF), and later the faster weakening and earlier dissipation of the primary eyewall. Reducing diabatic heating in ORBs weakens the rainbands and delays the SEF but prolongs the duration of the double eyewall structure if the SEF occurs. Reducing diabatic cooling in ORBs enhances convective activity in rainbands but has little effect on convection in the primary eyewall prior to the SEF. However, it results in a widened eyewall structure and a stronger TC after the eyewall replacement. Increasing diabatic cooling in ORBs largely suppresses convection in rainbands and prohibits the SEF. These results demonstrate that diabatic heating/cooling in ORBs plays important roles in the SEF and evolution. Since diabatic heating/cooling in rainbands is sensitive to the near-core environmental relative humidity, our results demonstrate the critical importance of large-scale environmental moist condition to the formation and evolution of secondary eyewall in TCs. In addition, it is also found that when the area-averaged diabatic heating rate in ORBs becomes similar in magnitude to that in the primary eyewall, the secondary eyewall forms.

Plain language summary: Previous studies have demonstrated the importance of diabatic heating/cooling in outer rainbands to the structure and intensity changes of tropical cyclones (TCs) with a single eyewall. It is unclear whether and how diabatic heating/cooling in outer rainbands may affect the formation and evolution of the secondary eyewall in TCs. These issues have been addressed based on a series of sensitivity experiments under idealized conditions using a high-resolution atmospheric model. Results show that diabatic heating in outer rainbands is favorable for the secondary eyewall formation (SEF). Increasing diabatic heating in outer eyewall can lead to faster weakening and thus earlier dissipation of the primary eyewall. Diabatic cooling in outer

rainbands suppresses convection in outer rainbands and prohibits the SEF. Since diabatic heating/cooling in outer rainbands is sensitive to the near-core environmental relative humidity, our results demonstrate the importance of the large-scale environmental moist condition to the SEF of TCs. We also found that when the area-averaged diabatic heating rate in outer rainbands becomes similar in magnitude to that in the primary eyewall, the secondary eyewall would form, which can be considered as a measure of the SEF in TCs.

1. Introduction

The concentric (double) eyewall structure, which is characterized by a secondary eyewall forming outside the primary eyewall, is a distinct feature in intense tropical cyclones (TCs). The secondary eyewall formation (SEF) and the subsequent replacement of the primary eyewall by the secondary eyewall are often accompanied with a temporary weakening followed by a re-intensification (Willoughby et al., 1982; Black and Willoughby 1992; Hawkins et al., 2006; Houze et al., 2007). Observational studies have demonstrated that the SEF is often related to active outer spiral rainbands, the subsequent enhancement of convection and axisymmetrization to form a quasi-axisymmetric convective ring structure accompanied with a secondary tangential wind maximum in the lower troposphere (Willoughby et al., 1982; Hawkins, 1983; Black and Willoughby, 1992; Houze et al., 2007; Yang et al., 2013). Understanding the processes involved in the SEF and the associated eyewall replacement cycle (ERC) is essential for improving the accuracy of predictions regarding TC structure and intensity, which are critical for effective weather forecasting and disaster preparedness (Kossin and Stikowski, 2009, 2012; Kossin and DeMaria, 2016). It is key to understand what determines the duration of the double eyewall structure and the intensity change during the ERC.

Most previous studies have mainly focused on how spiral rainbands develop into a quasi-axisymmetric convective ring, or how the nascent secondary eyewall forms and intensifies. Meanwhile, some other studies have concentrated on the triggers for strong spiral rainbands to be integrated into the secondary eyewall. These triggers are either internal dynamics or external factors, such as vortex Rossby waves, the beta - effect, orographic forcing, and environmental vertical wind shear (e.g., Willoughby, 1979; Hawkins, 1983; Montgomery & Kallenbach, 1997; Nong & Emanuel, 2003; Terwey & Montgomery, 2008; Kuo et al., 2009; Qiu et al., 2010; Abarca & Corbosiero, 2011; Rozoff et al., 2012; Fang & Zhang, 2012; Menelaou et al., 2012; Huang et al., 2012, 2018; Kepert, 2013; Sun et al., 2013; Zhu & Zhu, 2014; Zhang et al., 2017; Zhang et al. 2018; Wang et al., 2016, 2019; Dai et al., 2017, Guimond et al., 2020; Wang and Tan 2020, 2022, ; Liu et al, 2022).

Observational studies have demonstrated the importance of both convective structure and the stratiform sector in spiral rainbands and their evolution to the SEF (Didlake and Houze, 2011, 2013a, b; Didlake et al. 2017; 2018; Wunsch and Didlake, 2018; Tyner et al. 2018; Fischer et al. 2020; Zhu et al, 2022). These studies found that the left-of-shear mesoscale descending inflow in the stratiform rainband complex occurs in a region of latent cooling and negative buoyancy. The descending inflow can initiate the coupling between the boundary layer and the upper troposphere. Persistent low-level updrafts are then triggered along the inner edge of the surface cold pool, locally accelerating the tangential wind prior to the SEF. Wang et al. (2019) demonstrated from their idealized numerical simulation that diabatic heating in outer rainbands (ORBs) may induce deep-layer inflow and bring the absolute angular momentum inward and spin up the tangential wind near and outside the ORBs. The perturbation radial and tangential winds spiral cyclonically inward and downward along the rainband, showing a "top-down" pathway to the SEF. Continuous downward/inward propagation and axisymmetrization of the downwind sector of the rainbands in the boundary layer eventually lead to the SEF. Several recent studies have also confirmed the mechanism (Yu et al., 2021).

Both observational studies and idealized numerical simulations have found that diabatic heating in ORBs enhances prior to the SEF. When the diabatic heating rate in ORBs reaches a certain magnitude, the ERC process begins (Zhu and Zhu, 2014; Wang et al., 2019). Chen (2018) examined the sensitivity of TC intensity and structure changes to the magnitude and radial location of the increased inner-core diabatic cooling rate during the SEF and ERC. They found that both a

40% increase and a 10-km radial outward shift of cooling could lead to the occurrence of active ORBs at a larger radius, resulting in the delay of the SEF. These limited studies seem to suggest that both diabatic heating and cooling in spiral rainbands play some important but different roles in triggering the SEF and the subsequent intensity change during the ERC. However, a systematic study focusing on the roles of diabatic heating/cooling prior to and during the SEF is lacking so far. Questions remain unclear, including how diabatic heating affects the timing of the SEF, the duration of the double eyewall structure, and the structure and intensity changes during the ERC.

Numerous studies have devoted to the roles of diabatic heating/cooling in spiral rainbands in affecting the intensity and structure changes of single-eyewall TCs based on either balanced vortex dynamics or full-physics numerical simulations (Wang, 2009; Vigh & Schubert, 2009; Pendergrass & Willoughby; 2009; Moon & Nolan, 2010; Fudeyasu & Wang, 2011; Li et al., 2014; Navarro et al., 2017). These studies have confirmed that diabatic heating/cooling, regardless in the inner or ORBs, can lead to significant structure and intensity changes by affecting the secondary circulation. Among these studies, Wang (2009) demonstrated the importance of enhanced diabatic heating in ORBs to the SEF. Motivated by previous studies on the SEF and the earlier study of Wang (2009) and Li et al. (2014), in this study, we attempt to systematically investigate how the timing of the SEF and the duration of double eyewall structure, and the associated structure and intensity changes would be affected by diabatic heating/cooling in ORBs (or the outer eyewall) on the simulated ERC under idealized conditions. This was done following Wang (2009) by artificially modifying the diabatic heating/cooling rate in ORBs prior to and during the SEF. The rest of the article is organized as follows. The model used and the experimental design are briefly introduced in section 2. Section 3 presents an overview of the simulated SEF in the control experiment. Results from the sensitivity experiments both well before and shortly prior to the SEF in the control experiment are analyzed in section 3. Main conclusions are summarized and discussed in section 4.

2. Model and experimental design

We employed the widely used Weather Research and Forecasting (WRF) model, version 4.2.1

(Skamarock et al., 2008) in this study. The model configurations were basically the same as those utilized in Wang et al. (2016, 2019). The model domain was quadruply nested with the horizontal resolutions of 45, 15, 5, and 1.67 km, respectively, to achieve high-resolution in the TC inner core and the active spiral rainbands. The model atmosphere had 50 vertical levels extending from the surface up to 50 hPa. The four domains consisted of 200×200, 250×250, 268×268, and 388×388 grid points. The three inner nested domains moved automatically with the TC center. The innermost domain was large enough to cover the TC inner core, including the eyewall and both inner and outer rainbands. The model physics comprised the Yonsei University (YSU) planetary boundary layer scheme (Noh et al. 2003), the WRF single-moment 6-class microphysics scheme (Hong et al. 2006), the shortwave radiation scheme of Dudhia (Dudhia 1989), the Rapid Radiative Transfer Model (Mlawer et al. 1997). The Kain–Fritch cumulus parameterization scheme (Kain and Fritsch 2004) was applied only in the two outer domains.

The model was initialized with an axisymmetric TC-like vortex (Wang, 2007) on an *f*-plane (a constant Coriolis parameter) at 20°N with a constant sea surface temperature (SST) of 29°C. The initially unperturbed environmental sounding was that of the western Pacific clear-sky environment given in Gray et al. (1975). The maximum tangential wind in the initial axisymmetric cyclonic vortex was 45 m s^{-1} at the radius of 60 km at the surface and decreases sinusoidally with height and became zero at 100 hPa, and the tangential wind speed decreased to zero at the 1000-km radius. The TC vortex was initially in hydrostatic and gradient wind balances and was located at the center of each domain.

Following the approach of Wang (2009) and Li et al. (2014), several sensitivity experiments (Table 1) were conducted by artificially modifying the diabatic heating rate (Q) from the cloud microphysics scheme in the WRF model. The total Q at a given time step at a grid point in three dimensions can be decomposed into diabatic heating rate (Q_+) and diabatic cooling rate (Q_-):

$$Q = Q_+ + Q_- = \max(Q, 0.0) + \min(Q, 0.0). \quad (1)$$

The radius of 70 km was selected as the innermost edge of the ORBs and the outermost of the primary eyewall (the outer edge of the anvil clouds of the primary eyewall) and inner rainbands.

Only Q in the ORBs was modified to examine the effects of diabatic heating and cooling on the rainband activities and the accompanied SEF and ERC processes. To reduce the discontinuity in diabatic heating rate at the radius of 70 km, a linear transition zone was applied to the radial range between the radii of 65–70 and 70–75 km, respectively. The vortex center, which was defined as the circulation center, was determined at each time step to ensure the accurate modifications to diabatic heating/cooling in ORBs.

Table1. Summary of the numerical experiments conducted in this study, with r being the radius from the TC center, which is defined as the circulation center at the lowest model level.

Exp.	Comments on the experimental design
CTRL	The default model settings.
HC0.9	Both the Q_+ and Q_- are reduced to 90% outside r=70 km.
HC0.95	Both the Q_+ and Q_- are reduced to 95% outside r=70 km.
HC1.05	Both the Q_+ and Q_- are increased by 5% outside r=70 km.
HC1.1	Both the Q_+ and Q_- are increased by 10% outside r=70 km.
H0.9	Only the Q_+ is reduced to 90% outside r=70 km.
H0.95	Only the Q_+ is reduced to 95% outside r=70 km.
H1.05	Only the Q_+ is increased by 5% outside r=70 km.
H1.1	Only the Q_+ is increased by 10% outside r=70 km.
C0.9	Only the Q_- is reduced to 90% outside r=70 km.
C0.95	Only the Q_- is reduced to 95% outside r=70 km.
C1.05	Only the Q_- is increased by 5% outside r=70 km.
C1.1	Only the Q_- is increased by 10% outside r=70 km.

In the control experiment (CTRL), all default model settings were adopted. Two sets of sensitivity experiments were performed with initial conditions from CTRL but after different times of model run. One set of experiments started after 96 h of the simulation in CTRL, well before the SEF in CTRL, and the other set of experiments started after 120 h of the simulation in CTRL, shortly prior to the SEF in CTRL. Three groups of experiments were conducted for each set. In the first group, both diabatic heating and cooling rates increased by 5% outside the radius of 70 km in HC1.05 and 10% in HC1.1 and reduced by 5% in HC0.95 and 10% in HC0.9. In the second group, only the diabatic heating rate increased by 5% in H1.05 and 10% in H1.1 and reduced by 5% in H0.95 and 10% in H0.9. In the third group, only the diabatic cooling rate increased by 5% in C1.05

and 10% in C1.1 and reduced by 5% in C0.95 and 10% in C0.9. Therefore, in addition to CTRL, 12 sensitivity experiments in total (Table 1) were conducted to understand the role of diabatic heating/cooling in ORBs in the timing of the SEF, the duration of the double eyewall structure, and the associated intensity changes. Note that if the outer eyewall formed outside the 70-km radius, the diabatic heating/cooling rate in the outer eyewall were also modified, which may enhance the outer eyewall convection and the contraction of the outer eyewall, and thus the weakening and dissipation of the primary eyewall. The artificially modifying diabatic heating/cooling in the outer rainband region can also directly modifying the activity of outer spiral rainbands. Therefore, the consequence due to changes in diabatic heating/cooling rate can also be considered as a result of changing outer rainband activity in sensitivity experiments. Note also that increasing diabatic heating rate in outer rainbands is equivalent to increasing moisture content in the TC near-core environment, while increasing the diabetic cooling rate is equivalent to having a dry near-core environmental condition or dry air intrusion as discussed in Wang (2009).

3. Results

a. An overview of the SEF in the control experiment

Figure 1 shows the intensity evolutions of the simulated TCs in all experiments listed in Table 1 in terms of the maximum near-surface wind speed. Here, we first discuss the intensity evolution of the TC in CTRL. After an initial spinup period of about 48 hours, the simulated TC achieved a maximum wind speed of approximately 48 m s^{-1}. The TC then steadily intensified for 24 h, and reached its quasi-steady evolution with moderate intensity oscillations. The TC weakened from 126 h (approximately 9 hours prior to the SEF) to 150 h (the completion of the ERC), followed by a weak intensification followed by an intensity oscillation until the end of the 192-h simulation. Figure 2 presents the simulated radar reflectivity at the 3-km height prior to and during the onset of the SEF at 3-hour intervals. By 96 h, the TC presented an eyewall at a radius of about 40 km, surrounded by scattered convective activities outside the eyewall. The scattered convective activities were then organized into spiral rainbands. By 111 h, a main spiral rainband progressively formed around a radius of 150 km to the south and west of the TC center. The rainband spiraled cyclonically inward and intensified, but gradually stagnated at a radius of about 100 km and continued strengthening around this radius. The spiral rainbands eventually evolved into a nearly closed convective ring at approximately 100 km by 117 h, along with the formation of the clear moat structure. Based on the definition commonly used in previous studies, namely the time when the secondary maximum in the azimuthally averaged tangential wind appears, the outer eyewall formed completely by 135 h. With further intensification and contraction of the outer eyewall, the inner eyewall weakened and eventually dissipated after about 150 h of the simulation.

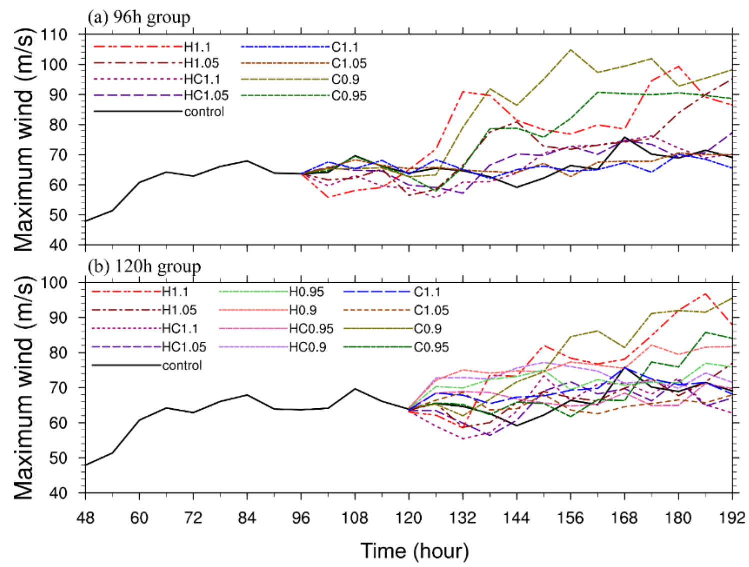

Figure 1. Time evolution of the simulated TC intensity in terms of the maximum near-surface wind speed (m s^{-1}) in CTRL and all sensitivity experiments initiated after (a) 96 h and (b) 120 h of the simulation in CTRL.

Figure 3 shows the time-radial cross-sections of the azimuthal-mean radar reflectivity at 3-km height and vertical motion and tangential wind speed at 1.5-km height in CTRL. The evolution of radar reflectivity and vertical motion indicates deep convection in the primary eyewall, which remained at the radius of about 40 km after 72 h of the simulation (Fig. 3a). The radius of maximum wind (RMW) was located between 30 and 40 km radii with a maximum wind speed over 70 m s^{-1} after 72 h of the simulation (Fig. 3b). By 111 h, scattered updrafts developed outside a radius of 120 km, indicating the development of ORBs and the formation of weak convective ring structure. These ORBs propagated radially inward and eventually evolved into a nearly axisymmetric structure by 135 h. The TC inner-core size showed a steady increase as seen from the contour of 40 m s^{-1} tangential wind speed, showing an outward expansion, consistent with the development of ORBs after 111 h. As the tangential wind expanded outward and accelerated, updrafts in ORBs organized into a convective ring after 120 h, a secondary maximum in tangential wind speed started to develop with the strengthening of the outer convective ring. The secondary peak in upward motion (larger than 0.5 m s^{-1}) and a clear secondary tangential wind maximum appeared by 135 h, indicating the SEF. With the strengthening and contraction of the outer eyewall, the inner eyewall began to weaken and eventually dissipated by around 150 h. The double eyewall structure maintained for about 15 h.

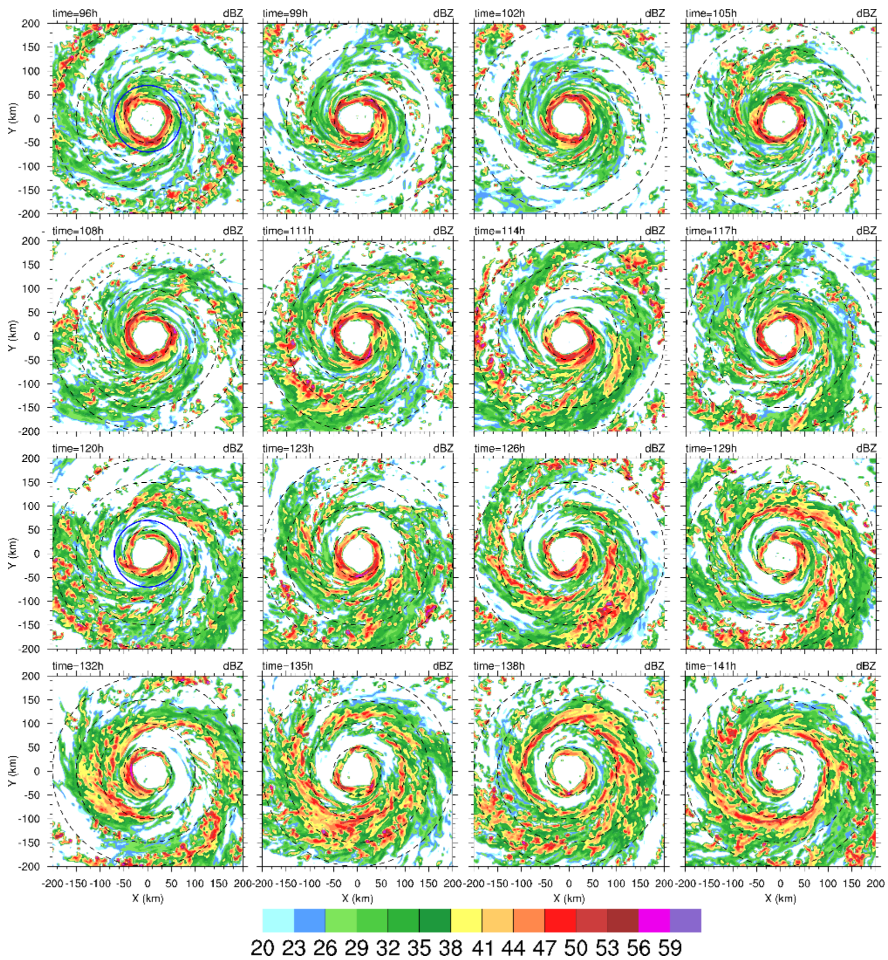

Figure 2. Plan view of radar reflectivity (shaded; dBZ) at a 3-km height from 96 to 141 h at 3-h interval in CTRL with the model time given at the top of each panel. The four concentric circles denote the radii of 50, 100, 150, and 200 km from the TC center in each panel. A blue circle is placed at the 70-km radius circle for 96 h and 120 h, namely the times the two sets of sensitivity experiments started.

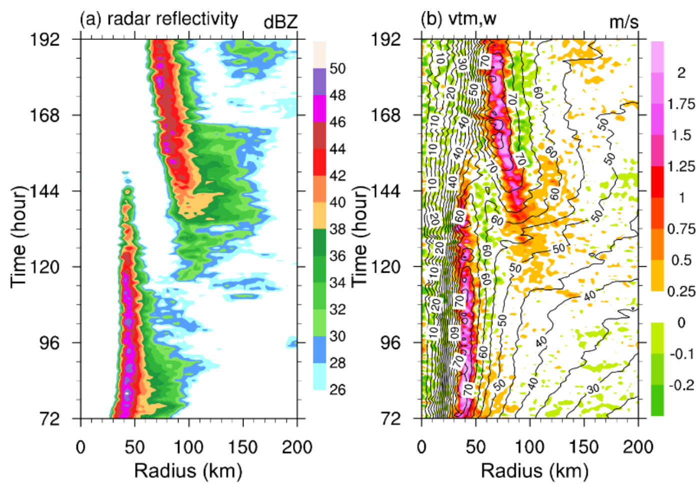

Figure 3. Time-radius Hovmöller diagrams of the azimuthally averaged (a) radar reflectivity at 3 km (dBZ), (b) vertical motion at 3 km (shaded, m s^{-1}) and tangential wind speed at the 1.5-km height (contours, m s^{-1}) from 72 to 192 h in CTRL.

The development of ORBs and the associated SEF can be further viewed in the radius–vertical cross sections of the azimuthally averaged diabatic heating rate and tangential wind speed given in Fig. 4. At 96 h (Fig. 4a), a single eyewall was located between radii of 30–40 km of the TC center and sloped outward with height. Strong diabatic heating occurred in the primary eyewall. Diabatic cooling appeared both inside and outside the primary eyewall. The region with diabatic cooling gradually evolved into the moat area as the ORBs (and later the outer eyewall) intensified. Diabatic heating outside the primary eyewall was not pronounced until the enhancement of ORBs around the radii between 130–160 km by 111 h, especially above the 2-km height. The continuous strengthening of diabatic heating in ORBs coincided with the outward tangential wind expansion, indicating that the latter was closely related to diabatic heating in ORBs. Diabatic heating outside a radius of 150 km progressively shifted inward and strengthened after 111 h and slowed down and remained between radii of 70–120 km. During 117–132 h, diabatic heating in the ORB region became stronger and better organized, implying the continuous axisymmetrization of ORBs. By 135 h, diabatic heating showed a sudden enhancement with a clear convective ring structure as also seen from Fig. 2, together with the appearance of a secondary tangential wind maximum between 70–90 km radii, indicating the SEF. The primary eyewall convection weakened and eventually disappeared, and the secondary eyewall contracted inward gradually and intensified.

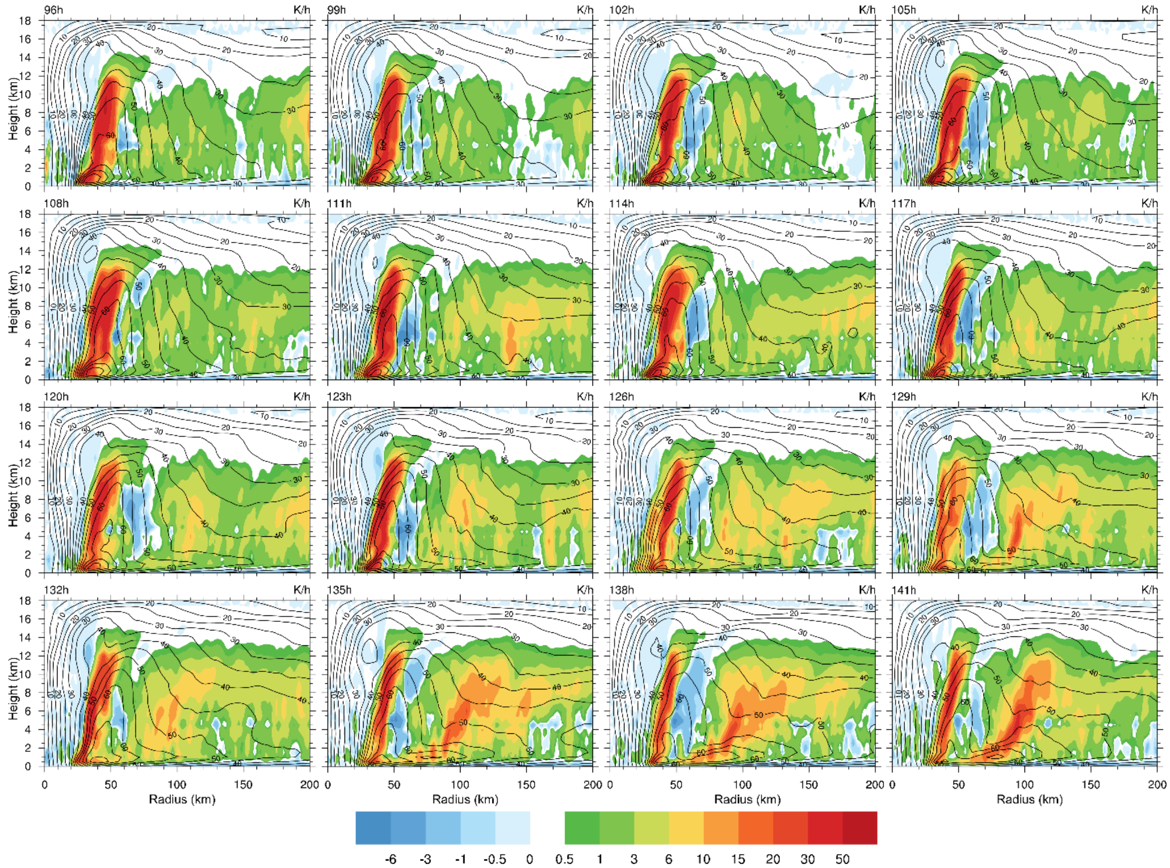

Figure 4. Radius–height cross sections of the azimuthal mean tangential wind speed (contour, m s^{-1}) and diabatic heating rate (shaded, K h^{-1}) in CTRL. Model time is given at the top left of each panel.

b. Modified heating/cooling well before the SEF

Based on the above analysis, ORBs were inactive before 96 h but became active about 111 h of the simulation, resulting in the SEF in about 24 h (by 135 h). Therefore, diabatic heating/cooling outside a radius of 70 km at 96 h can be regarded as the region with ORBs (Figs. 3 and 4). We thus conducted sensitivity experiments by artificially modifying the diabatic heating rate outside the radius of 70 km to understand the role of diabatic heating in ORBs in affecting the timing of the SEF and duration of the double eyewall structure simulated in CTRL. Eight sensitivity experiments were carried out with the diabatic heating rate modified after 96 h of the simulation in CTRL (Table 1). Figure 1a shows the time evolution of the maximum wind speed for all eight sensitivity experiments. Note that HC0.95 and HC0.9 and H0.95 and H0.9 were not shown here because reducing the diabatic heating rate resulted in too weak ORBs with no SEF.

The concurrent increase in both diabatic heating and cooling rates outside the primary eyewall led to the earlier SEF and the persistent weakening of the TC in the first 36 h of the simulation in HC1.05 (Fig. 5a and Table 2) and in the first 30 h of the simulation in HC1.1 (Fig. 1a). Note that the time in our following discussion is referred to the time from the modification of diabatic heating in sensitivity experiments. TCs in both experiments intensified again after the completion of the ERC during 36–48 h of the modified diabatic heating in HC1.05 and during 30–60 h in HC1.1. Eventually, a quasi-steady intensity achieved and maintained until the end of the simulations. Increasing diabatic heating rate only led to the greatest weakening of the TCs in the first 24 h of the simulation in H1.05 and in the first 6 h of the simulation in H1.1, both much earlier than in HC1.05 and HC1.1. This was followed by the greatest intensification from 24 to 48 h in H1.05 and from 6 to 36 h in H1.1, and then a moderate intensity oscillation thereafter. The results indicate that diabatic heating in ORBs can significantly affect the TC intensity by controlling the timing of the SEF and the duration of the double eyewall structure. The TC intensity evolution in C0.9 and C0.95 with reduced diabatic cooling rate was similar to that in CTRL in the first 48-h simulation, and then underwent a slight weakening for 6 hours. A gradual intensification began after 54 h until 120 h of the simulation in C0.9 and after 66 h of the simulation in C0.95, and the TCs eventually reached their quasi-steady states in both experiments. In contrast, the TCs with the increased diabatic cooling rate in ORBs in both C1.05 and C1.1 intensified and maintained a higher quasi-steady intensity due to the inactive ORBs and the absence of the SEF. All TCs in H1.05, H1.1, C0.9, and C0.95 reached a final intensity comparable to that in CTRL. TCs in HC1.05, HC1.1, H1.05, H1.1, C0.9, and C0.95 experienced the SEF and subsequent ERC, showing the weakening of the TC accompanied by the SEF and re-intensification after the completion of the ERC.

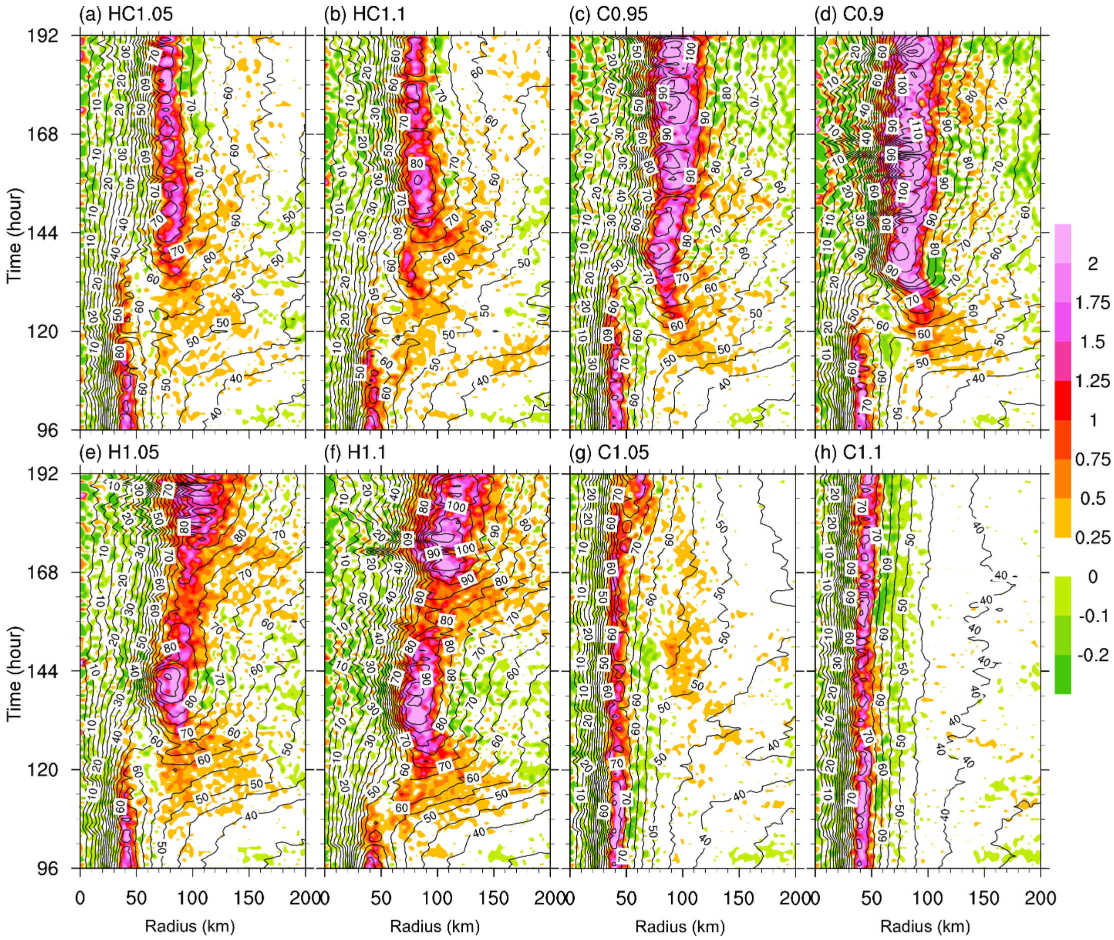

Figure 5. Time-radius Hovmöller diagrams of the azimuthal-mean tangential wind speed at 1.5-km height (contours, m s^{-1}) and vertical motion at 3 km (shaded, m s^{-1}) from (a) HC1.05, (b) HC1.1 (c) C0.95, (d) C0.9, (e) H1.05, (f) H1.1, (g) C1.05, and (h) C1.1, respectively.

Figure 5 compares the time evolution of the azimuthal-mean vertical motion at the 3-km height and tangential wind speed at the 1.5-km height in the eight sensitivity experiments. The timing of the SEF and the duration of the double eyewall structure in those corresponding experiments with the ERC are listed in Table 2. Substantial differences in vertical motion are present among the experiments with different modifications to diabatic heating/cooling in ORBs. In HC1.05 and HC1.1 with the diabatic heating and cooling rates increased (Figs. 5a, b), convective activities are discernible outside the eyewall after 6 h of the simulations and gradually developed afterwards, consistent with the initial weakening of the TCs. Convective activities in ORBs gradually strengthened and evolved into a strong convective ring, accompanied by the appearance of a local azimuthal-mean tangential wind maximum by 130 h in HC1.05 and by 128 h in HC1.1, indicating the earlier SEF than in CTRL (135 h). The duration of the double eyewall structure is 8 hours in HC1.05 and about 4 hours in HC 1.1 (Table 2). The results are understandable because enhancing diabatic heating and cooling in ORBs speeds up the SEF and the intensification of the outer eyewall (after its formation), suppressing the inner eyewall, leading to an earlier weakening and dissipation of the inner eyewall. In both HC1.05 and HC1.1, the outer eyewall remained at the radii of 70–80 km, similar to that in CTRL.

The evolution of the TCs in H1.05 and H1.1, with increased diabatic heating rate only (Figs. 5e, f), resembles those in HC1.05 and HC1.1 in the early stages with convective activities developing after the first 6 h of the simulations. The secondary eyewall formed at around 122 h in H1.05 (Fig. 5e) and at around 110 h in H1.1. Different from those in HC1.05 and HC1.1, the inner eyewall weakened and dissipated shortly after the SEF in both H1.05 and H1.1. This indicates that the enhanced diabatic heating rate in ORBs weakened the primary eyewall and accelerated the formation and intensification of the outer eyewall, giving rise to the rapid weakening and dissipation of the inner eyewall and shortening the duration of the double eyewall structure. Different from that in HC1.05, HC1.1, and CTRL, convective ring of the eyewall after the ERC in H1.05 and H1.1 is much stronger and wider and shows a gradual outward expansion with time. The SEF and evolution with the increased diabatic heating rate in ORBs (and later in the outer eyewall) are similar to that discussed in Wang (2009), who also simulated the SEF and the subsequent ERC with the diabatic heating rate artificially increased in ORBs.

With the reduced diabatic cooling rate in C0.95 and C0.9 (Figs. 5c, d), the SEF and the ERC show great similarity to those in H1.05 and H1.1, with the SEF occurring after 116 h of the simulation in C0.95 and 114 h in C0.9, much earlier than that in CTRL. The inner eyewall dissipated by 130 h in C0.95, resulting in a 14-h duration of the double eyewall structure, and by 120 h in C0.9, resulting in a duration of the double eyewall structure for only 6 h (Table 2). This indicates that the duration of the double eyewall structure is greatly shortened with the reduced diabatic cooling rate in the outer eyewall. Like that in experiments with the increased diabatic heating rate in H1.05 and H1.1, the replaced eyewall became wider and stronger than that in CTRL and HC1.05 and HC1.1, and also showed a slow outward expansion after the completion of the ERC with the strongest TCs in C0.95 and C0.9 (Fig. 2a). This indicates that diabatic cooling in ORBs suppresses the TC intensity, as also indicated in Wang (2009). Finally, increasing diabatic cooling rate in ORBs in C1.05 and C1.1 (Figs. 5g, h) suppressed convective activities in ORB, leading to the single eyewall structure throughout the simulations.

Table2. Summary of the time of SEF, the ending time of ERC, and the duration time in different experiments.

EXP（96h）	**SEF**	**ERC**	**Duration time**
CTRL	135 h	150 h	15 h
HC1.05	130 h	138 h	8 h
HC1.1	128 h	132 h	4 h
H1.05	122 h	122 h	0 h
H1.1	110 h	110 h	0 h
C0.95	116 h	130 h	14 h
C0.9	114 h	120 h	6 h
C1.05	--	--	--
C1.1	--	--	--

The above results indicate that increasing diabatic heating rate in ORBs can lead to the strengthening of convective activities in ORBs, resulting in the weakening of the primary eyewall and accelerating the SEF and ERC. Reducing diabatic cooling in ORBs can enhance convection in ORBs but has insignificant effect on the intensity of the primary eyewall prior to the SEF and leads to a stronger TC after the completion of the ERC. However, increasing diabatic cooling in ORBs would suppress convective activity in ORBs, preventing the SEF. To further understand how the modified diabatic heating rate in ORBs affects the simulated TC intensity change during the SEF and ERC, we examined the secondary circulation response to the difference in diabatic heating rate between each of the sensitivity experiments and CTRL. The model output in the 2-h period from 107 to 109 h of the simulations at 6-min intervals were used in the diagnostics.

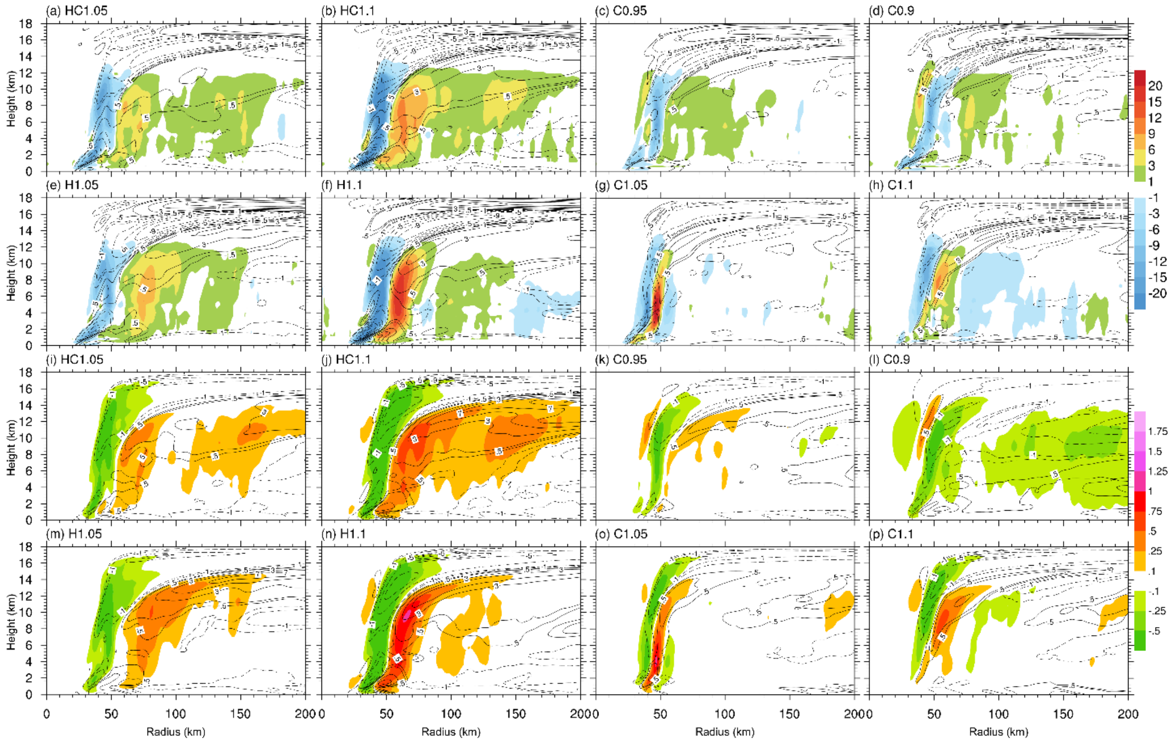

Figure 6. Upper two rows: the radius-vertical cross-sections of the differences in the azimuthal-men diabatic heating rate (shaded, K) and radial wind speed (contours, m s^{-1}) between the sensitivity experiments and CTRL from the WRF model output in the 2-h period from 107 to 109 h of the simulations based on model output at every 6 minutes (upper two rows) and the radius–vertical cross-sections of the vertical motion (shaded, m s^{-1}) and radial wind speed (contours, m s^{-1}) diagnosed using the Sawyer–Eliassen equation in response to the given difference in diabatic heating rate in the corresponding upper rows (lower two rows). The contours are ±15, ±13, ±11, ±9, ±7, ±5, ±3, ±1, ±0.5 m s^{-1}.

Figure 6 shows the differences in the azimuthal mean diabatic heating rate and radial wind speed between each of the sensitivity experiments and CTRL averaged over the chosen 2-h period. Increasing both diabatic heating and cooling rates in ORBs in HC1.05 and HC1.1 (Figs. 6a, b) led to a moderate increase in diabatic heating rate between 100 and 150 km from the TC center and also a couplet of reduced and increased diabatic heating rate across the radius of 50 km. The latter indicates an outward shift of the primary eyewall. In response to the increased diabatic heating rate in ORBs are the increase in both the boundary layer inflow and the upper-level outflow outside the ORBs but the decreased boundary layer inflow and upper-level outflow in the inner eyewall relative to those in CTRL. Note that an inflow layer appears immediately outside the enhanced diabatic heating region below about 10-km height, which brings absolute angular momentum inward and is responsible for the outward tangential wind expansion prior to the SEF.

The diabatic heating rate between radii of 90 and 180 km is much larger in both H1.05 than in H1.1 than in CTRL (Figs. 6e, f), indicating much stronger ORBs than in CTRL and also in both HC1.05 and HC1.1. This suggests that the increased diabatic cooling rate partially suppressed effect of the increased diabatic heating rate in HC1.05 and HC1.1. The relatively smaller diabatic heating rate inside a radius of 75 km implies the weaker convection in the primary eyewall in H1.05 and H1.1, consistent with the finding of Wang (2009), who also found that increasing diabatic heating rate in ORBs often led to the weakening of eyewall convection, leading to a weaker TC. Note that both HC1.1 and H1.1 show relatively larger outward shifts of the primary eyewall than HC1.05 and H1.05, as inferred from the larger couplets of the negative and positive diabatic heating rate differences (Figs. 6a, b, e, f). In response to the changes in diabatic heating rate in the primary eyewall, the low-level inflow and upper-level outflow near the primary eyewall greatly weakened compared to those in CTRL. The increased diabatic heating rate in ORBs substantially enhanced the boundary layer inflow under the ORBs as well as the inflow in a deep layer below 10-km height outside the increased heating region. This led to the earlier outward tangential wind expansion and the SEF in H1.05 and H1.1 (Figs. 5e, f).

Reducing diabatic cooling rate in ORBs in C0.95 and C0.9 (Figs. 6c, d) led to a slight decrease in diabatic heating rate in the primary eyewall and an increase in diabatic heating rate between the radii of 50–120 km compared with those in CTRL. Both the boundary layer inflow and the upper-level outflow decreased in the primary eyewall region. The low-level inflow increased in the outer region, especially outside a radius of 100 km where the ORBs were enhanced compared with those in CTRL. These changes suggest an earlier SEF in C0.95 and C0.9 than in CTRL (Figs. 5c, d). The increased diabatic cooling rate in C1.05 and C1.1 (Figs. 6g, h) led to the reduced diabatic heating rate in ORBs, suggesting a substantial weakening of ORBs. As a result, the SEF did not occur in either C1.05 or C1.1 (Figs. 5g, h). Note that the increased diabatic cooling rate in ORBs also resulted in an increased diabatic heating rate in the primary eyewall, which also became narrower than that in CTRL, as seen from the negative differences in diabatic heating rate near the outer and inner edges of the eyewall heating (Figs. 6g, h). Consistently, both the boundary layer inflow and the upper-level outflow near the eyewall in C1.05 and C1.1 were enhanced compared with those in CTRL. Therefore, diabatic cooling in ORBs is unfavorable for convective activity in ORBs but may contribute to a more compact inner-core TC, as previously found in Wang (2009).

The above results strongly suggest that the difference in the secondary circulation between any of the sensitivity experiments and CTRL is largely attributed to the difference in diabatic heating in the simulations. We found that the change in the secondary circulation can be largely explained by the balance response to the change in diabatic heating/cooling. To verify this hypothesis, we examined the balanced responses of the secondary circulation to the heating difference between each of the sensitivity experiments and CTRL using the Sawyer–Eliassen (SE) equation widely used to examine the forced transverse circulation in TCs in response to the given diabatic heating or momentum forcing or both (Eliassen, 1951; Willoughby, 1979; Schubert & Hack, 1982; Fudeyasu & Wang, 2011). Previous studies have demonstrated that the balanced dynamics can reasonably capture the transverse circulation and the tangential wind spinup in the SEF region (Fang & Zhang, 2012; Sun et al., 2013; Zhu & Zhu, 2014; Wang et al., 2016; Qin et al., 2021). The details of the procedure used can be found in Wang et al. (2016). Note that although the balanced dynamics often underestimates the inflow and thus tangential wind tendency in the boundary layer, it can well capture the secondary circulation and the spinup of tangential wind above the boundary layer (Bui et al., 2009; Fudeyasu & Wang, 2011; Wang et al., 2016, 2019). Since our focus is on the tangential wind tendency contributed by the modified diabatic heating rate in the sensitivity experiment, to diagnose the balanced response using the SE equation is helpful to understand the role of diabatic heating/cooling in ORBs in the simulated SEF.

Comparing the upper and lower two rows in Fig. 6, we can see that the diagnosed radial wind using the SE equation can well capture the difference in radial wind between each of the sensitivity experiments and CTRL derived from model output. The diagnosed vertical motion compares well with the difference in diabatic heating rate between the sensitivity experiment and CTRL. Namely, the increase in diabatic heating rate corresponds to upward motion, while the decrease in diabatic heating corresponds to descending motion. Previous studies indicate an outward tangential wind expansion prior to the SEF, as also seen from Fig. 3b in CTRL and Fig. 5 in all sensitivity experiments. To quantify the balanced contribution of the modified diabatic heating rate in ORBs, we also diagnosed the tangential wind tendency using the diagnosed secondary circulation as shown in the lower two rows in Fig. 6. The azimuthal mean tangential wind budget equation is

$$\frac{\partial \bar{v}}{\partial t} = -\bar{u}\overline{\zeta_a} - \bar{w}\frac{\partial \bar{v}}{\partial z} + \overline{F_v}, \tag{1}$$

where overbar indicates the azimuthal mean of the corresponding qunatity, $\bar{v}$, $\overline{\zeta_a}$, and $\overline{F_v}$ are the azimuthal mean tangential wind, vertical absolute vorticity, and vertical diffusion (including surface friction), all are temporarily averaged between 107–109 h of the simulations using model outputs at 6-min inervals; and $\bar{u}$, $\bar{w}$ are the azimuthal mean and temporarily averaged radial wind and vertical motion between 107–109 h of the simulaitons either from the model output or from those diagnosed using the SE equation. As a result, we consider the left-hand side being the azimthal mean tangential wind tendency either from the model output or the the balanced response in our following discussion.

Figure 7 shows the tangential wind tendencies calculated from the balanced response to the diabatic heating difference between each of the sensitivity experiments and CTRL (upper two rows) and those calculated directly using the model output (lower two rows). We can see that although some discrepancies exist, the balanced response largely captures the tangential wind tendencies obtained from the model output. The large discrepancies are present mainly in the primary eyewall region where large truncation errors often exist. The balanced response also underestimates the azimuthal mean tangential wind tendencies in the lower boundary layer as pointed out in previous studies (Bui et al., 2009; Heng et al. 2017). Nevertheless, the balanced dynamics well reproduces the azimuthal mean tangential wind tendency in response to the diabatic heating difference in the ORB region. The positive tangential wind tendencies are largely induced by the inflow forced by the increased diabatic heating rate (Fig. 6). This suggests that the outward tangential wind expansion prior to the SEF in sensitivity experiments (Fig. 5) is largely driven by diabatic heating in ORBs, as also demonstrated in previous studies (Rozoff et al., 2012; Wang et al., 2016, 2019).

Modifying the diabatic cooling rate in C0.95, C0.9, C1.05 and C1.1 results in relatively small changes in diabatic heating rate because the diabatic cooling rate is often considerably smaller than diabatic heating rate (Figs. 6c, d, g, h). This also explains relatively small tangential wind tendencies in those experiments (Figs. 7c, d, g, h). Note that increasing diabatic cooling rate in ORB region in C1.05 and C1.1 results in overall weak negative tendencies in tangential wind outside the 7-km radius, which prevents the outward tangential wind expansion and thus the SEF (Figs. 5g, h).

The above analysis indicates that the balanced dynamics can capture the main processes associated with the SEF in the simulations. In particular, diabatic heating in ORBs drives the inflow and thus the positive tangential wind tendency immediately outside the region of the SEF. This caused the outward expansion of tangential wind and the increase in inertial stability and thus diabatic hating efficiency in driving the low-level tangential wind in the SEF region as demonstrated by Rozoff et a. (2012). As a result, increasing diabatic heating rate in ORBs in H1.05 and H1.1 resulted in earlier SEF (Figs. 5e, f). Reducing diabatic cooling in ORBs in C0.95 and C0.9 also led to somewhat earlier SEF (Figs 5c, d). In contrast, increasing diabatic cooling rate in C1.05 and C1.1 largely suppressed the convective activity in ORBs, leading to the absence of SEF. These findings thus further demonstrate that active ORBs and their corresponding diabatic heating are crucial to the SEF in TCs although some other processes may play some roles in details.

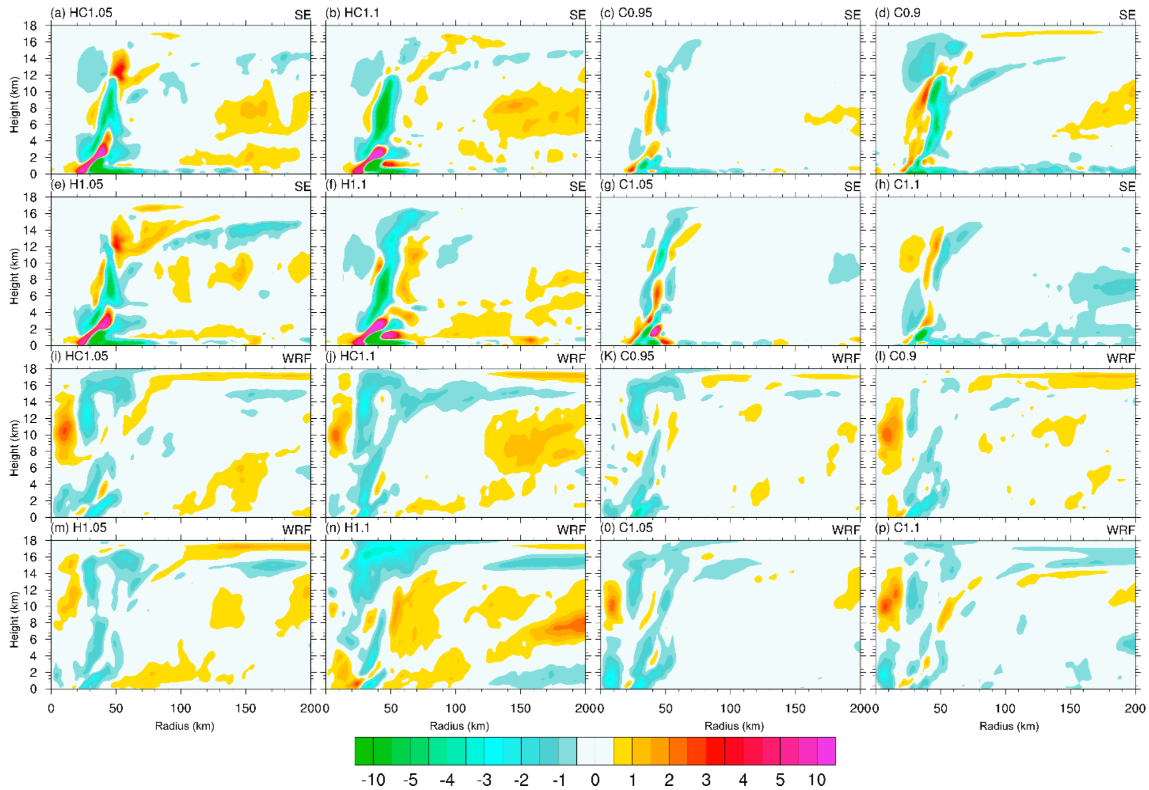

Figure 7. The azimuthal mean tangential wind tendency (shaded, m s^{-1} h^{-1}) diagnosed using the SE equation as the response to the change in the azimuthal mean diabetic heating rate between each of the sensitivity experiments and CTRL (upper two rows) and those calculated from the model output (lower two rows) between 107–109 of the simulation for all sensitivity experiments.

c. Modified heating/cooling shortly prior to the SEF

Shortly prior to the SEF in CTRL, ORBs became active from 111 h of the simulation in CTRL, and the azimuthally averaged tangential wind shows rapid broadening after 120 h (Figs. 2 and 3). Convective activities were concentrated with a thread-like structure at around 100 km radius. It is our interest to understand how the heating/cooling outside the radius of 70 km radius after 120 h of the simulation, about 15 hours prior to the SEF in CTRL may affect the formation and duration of the double eyewall structure and the subsequent eyewall replacement. For this purpose, we designed five groups of sensitivity experiments with the diabatic heating/cooling rate artificially modified from 120 h prior to the SEF in CTRL (see Table 1). The first three groups are similar to those discussed in section 3b. Two additional groups of experiments were carried out. In the fourth group, both diabatic heating and cooling rates were reduced by 5% in HC0.95 and 10% in HC0.9

outside the 70-km radius. In the fifth group, only the diabatic heating rate was reduced by 5% in H0.95 and 10% in H0.9 outside the 70-km radius. The evolutions of TC intensity in all sensitivity experiments are compared with the intensity evolution in CTRL in Fig. 1b. Note that the intensity evolution was closely related to the structure change, such as the SEF, the eyewall replacement, or dissipation of the newly formed outer eyewall without an eyewall replacement. Therefore, to better understand the intensity change, we show in Fig. 8 the time evolutions of the azimuthal mean tangential wind at 1.5 km and vertical motion at 3 km height from all sensitivity experiments. The timings of the SEF and the durations of the double eyewall structure for those experiments with TCs experiencing the ERC are listed in Table 3.

Table 3. Summary of the time of SEF, the ending time of ERC, and the duration time in different experiments with diabatic heating/cooling modified after 120 h of the simulation in CTRL.

EXP（96h）	SEF	ERC	Duration time
CTRL	135 h	150 h	15 h
HC0.9	166 h	--	--
HC0.95	138 h	180 h	52 h
HC1.05	132 h	138 h	6 h
HC1.1	126 h	132 h	6 h
H0.9	--	--	--
H0.95	--	--	--
H1.05	132 h	138 h	6 h
H1.1	126 h	130 h	4 h
C0.95	132 h	138 h	6 h
C0.9	132 h	136 h	4 h
C1.05	136 h	--	--
C1.1	--	--	--

From Fig. 1b, we can see that reducing both diabatic heating and cooling rates in ORBs led to an increase in TC intensity compared to that in CTRL. The intensity decreased during the SEF, which occurred after about 18 h in HC0.95 and 30 h in HC0.9, but re-intensified after the merging of the inner and outer eyewalls after about 60 h of the simulation in HC0.95 (Fig. 8a). The TC in HC0.9 weakened slowly afterwards because the outer eyewall was too weak to replace the inner eyewall (Fig. 8b). Reducing diabatic heating rate only in ORBs in H0.95 led to an increase in TC intensity up to 30 h of the simulation, followed by a decrease due to the SEF, and then a re-intensification after the dissipation of the secondary eyewall after 60 h of the simulation (Fig. 8c). Quite differently, the TC in H0.9 experienced an intensification until the end of the simulation with a single eyewall structure without active spiral rainbands (Fig. 8d), indicating that diabatic heating in ORBs or the outer eyewall suppresses the TC intensity. Consistent with the results in section 3b, increasing diabatic heating and cooling rates outside the 70-km radius resulted in the persistent weakening of the TC (corresponding to the SEF) in the first 18 h of the simulation in HC1.05 and 12 h of the simulation in HC1.1, and then both TCs intensified again (corresponding to the completion of the ERC) during 18–26 h in HC1.05 and 12–50 h in HC1.1 (Figs. 8e, f), which was followed by a quasi-steady intensity evolution until the end of the simulations (Fig. 1b). The TCs in H1.05 and H1.1 weakened greatly in the first 12 h of the simulations, followed by the greatest intensification until the end of the simulations. This means that the increased diabatic heating rate in outer eyewall accelerated the SEF and shortened the duration of the double eyewall structure, and thus is critical to TC intensity. The intensity evolution of the TC in C0.95 is similar to that in CTRL and shows a gradual intensification until the end of the simulation. The TC in C0.9 experienced a 12-h weakening and then intensified, achieving the strongest final intensity by the end of the simulation. The TC in C1.05 underwent two periods of intensification and then weakening, and then a quasi-steady evolution. The TC in C1.1 shows a quasi-steady evolution due to inactive ORBs and the absence of the SEF, reaching a steady-state intensity similar to that in CTRL.

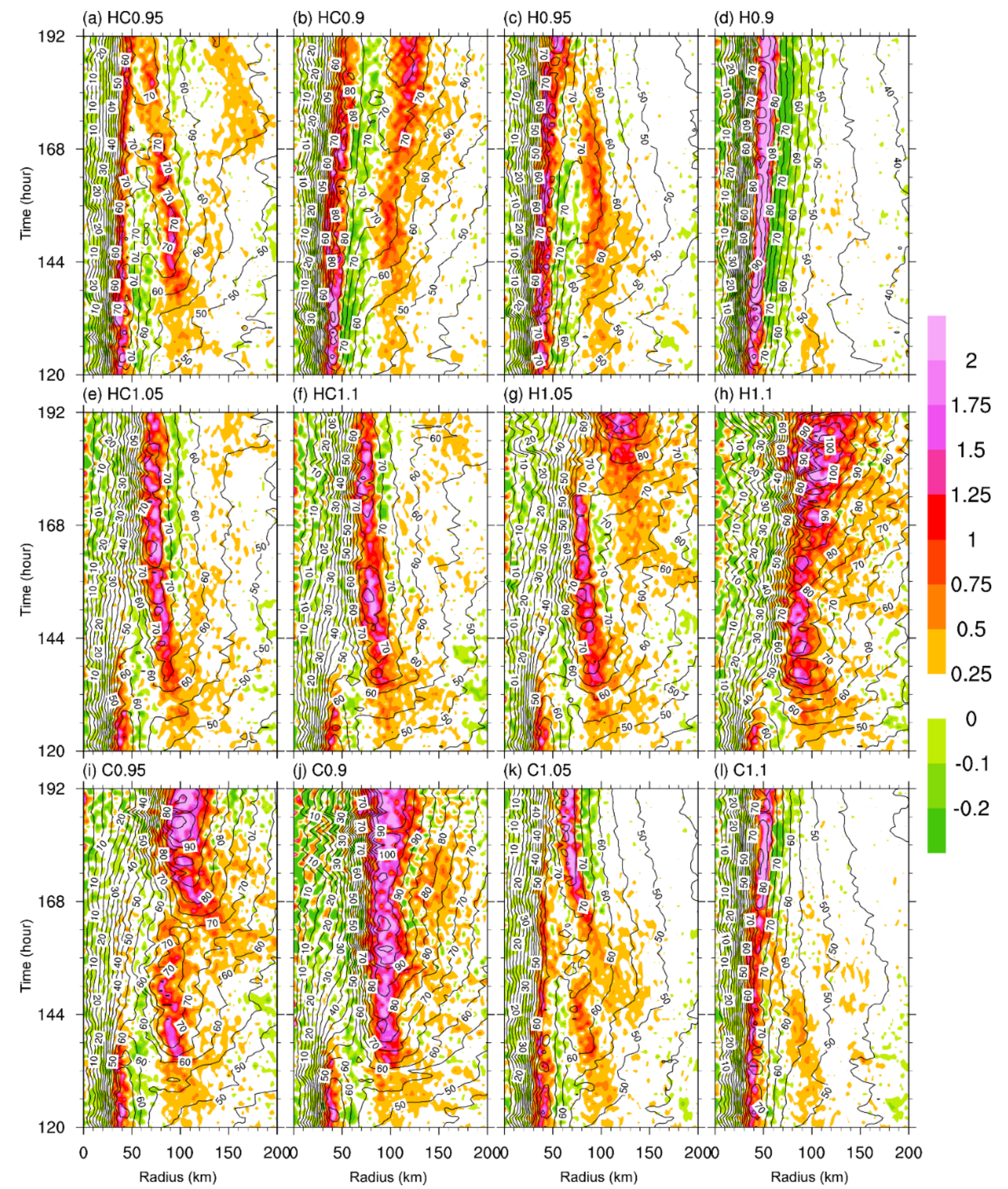

Figure 8. Time-radius cross-sections of the azimuthal mean vertical motion at 3-km height (shaded, m s^{-1}) and tangential wind at 1.5-km height (contours, m s^{-1}) from (a) HC 0.95, (b) HC0.9 (c) H0.95, (d) H0.9, (e) HC1.05, (f) HC1.1, (g) H1.05, (h) H1.1, (i) C0.95, (j) C0.9, (k) C1.05, and (l) 1.1, respectively.

With reduced diabatic heating and cooling rates in the outer eyewall region in HC0.95 and HC0.9, the inner eyewall persisted until the end of the simulations and both diabatic heating and cooling rates in the outer eyewall/rainband region continuously decreased (Figs. 8a, b). The secondary eyewall formed after about 18 h of the simulation in HC 0.95 and 46 h in HC0.9 (Table 3), and no eyewall replacement occurred in either case. The weaker convective activity in ORBs due to the reduced diabatic heating and cooling rates delayed the local tangential wind maximum appearance and the SEF. This suggests that the reduced diabatic heating rate in the outer eyewall imposed a less suppression to convection in the inner eyewall. The relatively weaker outer eyewall in HC0.9 even showed no obvious contraction and was not strong enough to suppress and replace the inner eyewall. With the diabatic heating rate only reduced in ORBs in H0.95 and H0.9, the inner eyewall did not only exist but also strengthened over time, especially in H0.9 (Figs. 8c, d). Weak rainbands were still visible in H0.95 but almost no active rainbands occurred in H0.9. The results confirm that diabatic heating in ORBs is crucial to the SEF and the subsequent eyewall replacement.

With both diabetic heating and cooling rates increased in HC1.05 and HC1.1 (Figs. 8e, f), convective activities in the ORB region strengthened with time, leading to the SEF at around 132 h of the simulation (Table 3), about 3 hours earlier than that in CTRL. The continuous intensification of the outer eyewall weakened the inner eyewall, leading to a quick dissipation of the inner eyewall. This considerably shortened the duration of the double eyewall structure to about 6 h in HC1.05 and even slightly less than 6 h in HC1.1. With only the diabatic heating rate increased in the ORB region (Figs. 8g, h), the secondary eyewall formed at 132 h in H1.05 and 126 h in H1.1, with the inner eyewall weakened and dissipated shortly after the SEF. The outer eyewall appeared at a relatively larger radius and was considerably wider in H1.1 than in CTRL, and also showed a continuous outward expansion and widening (Fig. 8h). Interestingly, a second SEF episode occurred in H1.05 after about 158 h of the simulation as the previous outer eyewall continuously contracted, with the second ERC completed by 180 h of the simulation (Fig. 8g). This is because increasing diabatic heating rate outside the previous outer eyewall enhanced the convective activity in ORBs, causing the second SEF and ERC episode.

Modifying diabatic cooling rate in the ORB region resulted in some distinct responses in the SEF and the ERC (Figs. 8i, j, k, h). As in H1.05, two episodes of SEF occurred in C0.95 (Fig. 8i), the first secondary eyewall formed at about 132 h with the inner eyewall dissipated after about 6 h of the simulation. The second secondary eyewall formed at about 162 h, with the inner eyewall dissipated in less than 6 h with a very large eyewall at around a radius of 100 km. In C0.9 (Fig. 8j), the secondary eyewall formed after about 132 h of the simulation, with the inner eyewall dissipated in about 4 h after the SEF. The outer eyewall continuously intensified and remained at a radius of about 100 km, leading to the TC intensification throughout the simulation (Fig. 2b). With the increased diabatic cooling rate in the ORB region in C1.05 (Fig. 8k), the TC also experienced two episodes of SEF. The first and second SEFs occurred at about 136 h and 156 h of the simulation, respectively. Note that the first episode did not result in the eyewall replacement. The outer eyewall in the first episode formed at a radius of around 100 km and showed a contraction as the inner eyewall weakened. However, active ORBs formed outside the outer eyewall, leading to the outer eyewall weakened and dissipated as the new ORBs organized into a new secondary eyewall by 156 h of the simulation. The original inner eyewall then gradually weakened and dissipated at about 168 h of the simulation. The increased diabatic cooling rate in C1.05 suppressed the activity of convection outside the new outer eyewall, resulting in a strong but narrow eyewall after the eyewall replacement. Further increasing the diabatic cooling rate in ORBs in C1.1 led to the weakening of ORBs. As a result, the TC remained a single eyewall structure throughout the simulation (Fig. 8l). This also resulted in a relatively stronger TC than that in CTRL (Fig. 2b).

The above results with diabatic heating artificially modified shortly prior to the SEF further confirm that diabatic heating in ORBs is key to active rainbands and the SEF and often shortens the duration of the double eyewall structure. Diabatic cooling in ORBs is unfavorable for convection in ORBs and thus suppresses the development of double eyewall structure. However, suppressed ORBs due to increased cooling favors the TC intensification and a relatively compact inner-core structure.

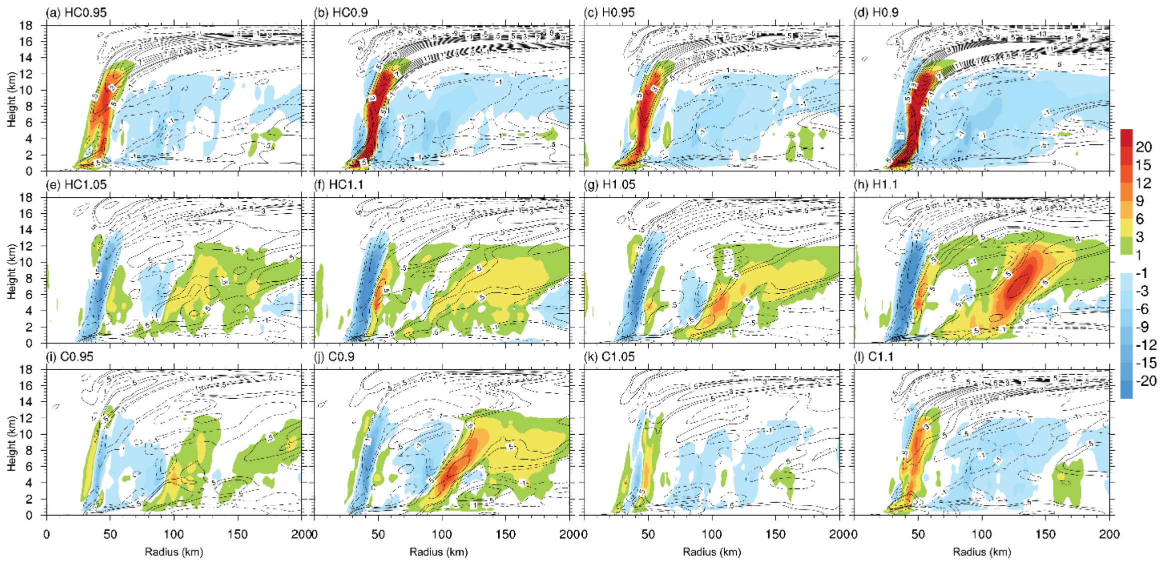

Figure 9. The differences in the azimuthally averaged the diabatic heating rate (shaded, K) and the radial wind (contour, m s^{-1}) between sensitivity experiments and CTRL from the WRF model. The contours are ±15, ±13, ±11, ±9, ±7, ±5, ±3, ±1, ±0.5 m s^{-1}.

To further illustrate the structure change in sensitivity experiments relative to that in CTRL, we shown in Fig. 9 the differences in the azimuthal mean diabatic heating rate and radial wind (sensitivity experiment minus CTRL) averaged over the 2-h period 131–133 h of the simulations based on the WRF model output at 6-minute intervals. Reducing both diabatic heating and cooling rates in ORBs in HC0.95 and H0.9 or diabatic heating only in H0.95 and H0.9 (Figs. 9a–9d) led to the weakening of ORBs and the strengthening of the inner eyewall heating, preventing the eyewall replacement or even the SEF. Increasing both diabatic heating and cooling rates in ORBs in HC1.05 and HC1.1 or diabatic heating only in H1.05 and H1.1 substantially enhanced convective activity in ORBs and the SEF. This led to suppressed convection in the inner eyewall and largely shortened the duration of the ERC, and even leading to the second episode of SEF, such as in H1.05 (Fig. 8g). Note that larger increased diabatic heating/cooling rate in HC1.1 and H1.1 also led to somewhat outward shift of the inner eyewall (Figs. 9f, h). The reduced diabatic cooling rate in C0.95 and C0.9 (Figs. 9i, j) resulted in an increase in diabatic heating rate in ORBs, indicating more active ORBs, the weakening of the primary eyewall, and the early SEF and short duration of the double eyewall structure. Increasing diabatic cooling rate in the ORB region in C1.05 and C1.1 (Figs. 9k, l) largely suppressed the activity of ORBs, as implied by the negative difference in diabatic heating rate outside the radius of 70 km. The increased diabatic heating rate in the inner eyewall region indicates intensification of the TC, especially in C1.1.

Changes in diabatic heating rate led to changes in the secondary circulation. As discussed in section 3b, in general, the reduced diabatic heating rate in ORBs results in enhanced boundary layer inflow into the inner eyewall region and the enhancement of the outflow in the upper troposphere, such as in HC0.95, HC0.9, H0.95 and H0.9 (Figs. 9a–9d). The increased diabatic heating rate in ORBs corresponds to the enhanced low-level inflow in the ORB region but the decreasing boundary layer inflow into the inner eyewall region and thus the weakened TC, such as in HC1.05, HC1.1, H1.05, H1.1 (Figs. 9e–9h). With the reduced (increased) diabatic cooling rate in the ORB region, ORBs would be strengthened (suppressed), leading to the enhanced (reduced) boundary layer inflow in the ORB region, while the reduced (enhanced) inflow toward the inner eyewall, such as in C0.95 and C0.9 (C1.05 and C1.1). Changes in the radial wind in the mid-lower troposphere show similarity to those discussed in section 3b for the sensitivity experiments initialized with the TCs well before the SEF in CTRL. Those changes can also be explained as a balanced response to changes in diabatic heating/cooling in ORBs as we discussed in section 3b.

4. Conclusions and discussion

Although it has been known that ORBs are critical to the SEF in intense TCs and the TC intensity changes during the subsequent ERC (e.g., e.g., Hawkins, 1983; Kuo et al., 2009; Wang et al., 2016, 2019; Yang et al. 2024), the role of diabatic heating/cooling in the SEF and the subsequent structural changes in TCs have not been systematically evaluated in the literature. This has been attempted here based on a series of sensitivity experiments using the high-resolution WRF model under idealized conditions by artificially increasing or decreasing diabatic heating/cooling rate in the ORB region in a control simulation. Results show that increasing diabatic heating rate in ORBs both before and shortly prior to the SEF resulted in the earlier SEF and the quick weakening of the eyewall, substantially shortening the duration of the double eyewall structure. Reducing diabatic heating rate in ORBs weakens the rainbands and delays the SEF, but prolongs the duration of the double eyewall structure if it develops. Reducing diabatic cooling rate in ORBs enhances convective activity in ORBs but has little effect on convection in the primary eyewall prior to the SEF. However, reducing diabatic cooling rate results in a wider eyewall structure and a stronger TC after the eyewall replacement. Increasing diabatic cooling rate in ORBs largely suppresses convection in rainbands and prohibits the SEF or leads to prolonged duration of the double eyewall if the outer eyewall already formed. Therefore, in general diabatic heating is key to the strengthening of ORBs, the outward expansion of tangential wind, and thus the SEF and the subsequent replacement of the inner eyewall by the outer eyewall. Diabatic cooling is unfavorable for convective activity in ORBs, prohibiting the outward expansion of tangential wind and thus negative to the SEF.

Our results strongly suggest that the relative magnitude of diabatic heating rates in ORBs and in the primary eyewall is crucial to the SEF and the eyewall replacement. To quantify this, we defined the ratio between the area-averaged diabatic heating rate in the eyewall and in ORBs. The area used in the average was the area in 20 km width centered at the maximum azimuthal mean diabatic heating rate vertically-averaged between 2–6 km heights in the eyewall or in the ORBs. Figure 10 shows the time series of the ratio so defined. The SEF in CTRL occurred at around 135 h as the ratio increased to approximately 1.0, indicating that the diabatic heating rates in ORBs and in the primary eyewall are comparable at the time of the SEF. After the SEF, the ratio often increased with time, indicating the strengthening of the outer eyewall and the weakening of the inner eyewall. However, the ratio could not imply the duration of the double eyewall structure because the inner eyewall dissipated at quite different rates as implied from the slope of the ratio in Fig. 10. Nevertheless, the ratio defined in this study can provide a quantitative measure to assess the likelihood of ORBs evolving into the outer eyewall in almost all experiments. Note that the measure of the relative heating rate between the primary eyewall and ORBs defined in this study is slightly different from the definition in Zhu and Zhu (2014), who selected the ratio of the maximum heating rates in ORBs and in the inner eyewall as the reference.

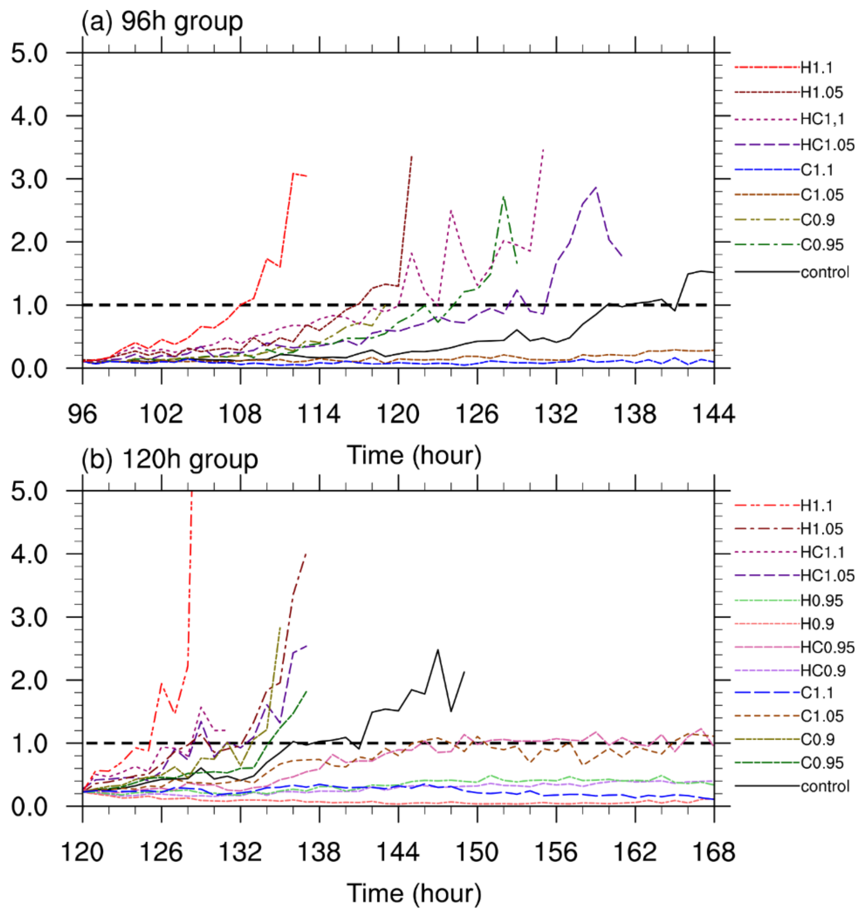

Figure 10. Ratio of the outer rainband heating rate to the inner eyewall heating rate between individual sensitivity experiments and CTRL. (a) Initialized sensitivity experiments well before the SEF in CTRL and (b) initialized sensitivity experiments shortly prior to the SEF in CTRL. Here the heating rate is area average in 20 km width centered at the maximum heating rate averaged between 2–6 km heights in the eyewall or the outer rainbands.

Diabatic heating /cooling in outer rainbands is affected by the near-core environmental relative humidity. High moisture content often favors diabatic heating, while dry near-core environmental conditions or dry air intrusion may promote diabatic cooling. In the western North Pacific region, as TCs are often influenced by the abundant water vapor in the western Pacific monsoon trough, most TC rainbands develop vigorously. As a result, most strong TCs would experience the ERC processes. Our finding can help to explain why the ERCs are more common in the western North Pacific than over the North Atlantic. We should also mention that although most previous studies have demonstrated the importance of ORBs to the SEF in TCs, no studies have examined the roles of diabatic heating/cooling in ORBs in determining the timing of the SEF and the duration of the double eyewall structure. Since diabatic heating/cooling in ORBs is associated with the near-core environmental moisture condition, our results can explain why the frequency of the secondary eyewall occurrence is much higher in the western North Pacific than in the North Atlantic. This is because over the western North Pacific, most TCs form in western Pacific monsoon trough with relatively higher moisture conditions in the mid-lower troposphere. However, over the North Atlantic, the lack of active monsoon trough and the effect of Saharan air layer produce a relatively drier environment, making the North Atlantic less favorable for the SEF than the western North Pacific. In addition, we should point out that the importance of diabatic heating/cooling in ORBs to the SEF and the structural change of the simulated TC is demonstrated from axisymmetric perspectives. The details of heating/cooling distribution in ORBs are not analyzed. For example, diabatic heating/cooling in ORBs may occur in convective and stratiform regions, which may have some different effects and could be studied in a future study.

***Acknowledgments*: This work was supported by the National Key R&D Program of China under grant 2022YFC3004200, the National Natural Science Foundation of China (42305007), and the S&T Development Fund of CAMS (2024KJ017). Y. Wang was supported by NSF grant AGS-1834300.

Data Availability Statement: All numerical experiments were conducted using the WRF model V4.2.1, which was downloaded from https://github.com/wrf-model/WRF/releases. All model outputs used in this study will be made available after the acceptance of the manuscript.

REFERENCES

Abarca, S. F., and K. L. Corbosiero, 2011: Secondary eyewall formation in WRF simulations of hurricanes Rita and Katrina (2005). *Geophys. Res. Lett.*, **38**, L07802, https://doi.org/10.1029/2011GL047015.

Black, M. L., and H. E. Willoughby, 1992: The concentric eyewall cycle of Hurricane Gilbert. *Mon. Wea. Rev.*, **120**, 947–957, https://doi.org/10.1175/1520-0493(1992)120<0947:TCECOH>2.0.CO;2.

Bui, H. H., R. K. Smith, M. T. Montgomery, and J. Peng, 2009: Balanced and unbalanced aspects of tropical cyclone intensification. *Quart. J. Roy. Meteor. Soc.*, **135**, 1715–1731, https://doi.org/10.1002/qj.502.

Chen, G., 2018: Secondary eyewall formation and concentric eyewall replacement in association with increased low-level inner-core diabatic cooling. *J. Atmos. Sci.*, 75, 2659–2685, https://doi.org/10.1175/JAS-D-17-0207.1.

Dai, Y., S. J. Majumdar, and D. S. Nolan, 2017: Secondary eyewall formation in tropical cyclones by outflow–jet interaction. J. Atmos. Sci., **74**, 1941–1958, https://doi.org/10.1175/JAS-D-16-0322.1.

Didlake, A. C., Jr., and R. A. Houze Jr., 2011: Kinematics of the secondary eyewall observed in Hurricane Rita (2005). *J. Atmos. Sci.*, **68**, 1620–1636, https://doi.org/10.1175/2011JAS3715.1.

Didlake, A. C., Jr., and R. A. Houze Jr., 2013a: Convective-scale variations in the inner-core rainbands of tropical cyclones. *J. Atmos. Sci.*, **70**, 504–523, https://doi.org/10.1175/JAS-D-12-0134.1.

Didlake, A. C., Jr, and R. A. Houze Jr, 2013b: Dynamics of the stratiform sector of a tropical cyclone rainband. *J. Atmos. Sci.*, **70**, 1891–1911, https://doi.org/10.1175/JAS-D-12-0245.1.

Didlake, A. C., Jr., G. M. Heymsfield, P. D. Reasor, and S. R. Guimond, 2017: Concentric eyewall asymmetries in Hurricane Gonzalo (2014) observed by airborne radar. *Mon. Wea. Rev.*, **145**, 729–749, https://doi.org/10.1175/MWR-D-16-0175.1.

Didlake, A. C., Jr., P. D. Reasor, R. F. Rogers, and W.-C. Lee, 2018: Dynamics of the transition from spiral rainbands to a secondary eyewall in Hurricane Earl (2010). *J. Atmos. Sci.*, **75**, 2909–2929, https://doi.org/10.1175/JAS-D-17-0348.1.

Dudhia, J., 1989: Numerical study of convection observed during the Winter Monsoon Experiment using a mesoscale two-dimensional model. *J. Atmos. Sci.*, **46**, 3077–3107, https://doi.org/10.1175/1520-0469(1989)046<3077:NSOCOD>2.0.CO;2.

Eliassen, A., 1951: Slow thermally or frictionally controlled meridional circulation in a circular vortex. *Astrophys*. Norv., **5**, 19–60.

Fang, J., and F. Zhang, 2012: Effect of beta shear on simulated tropical cyclones. *Mon. Wea. Rev.*, **140**, 3327–3346, https://doi.org/10.1175/MWR-D-10-05021.1.

Fischer, M. S., R. F. Rogers, and P. D. Reasor, 2020: The rapid intensification and eyewall replacement cycles of Hurricane Irma (2017). *Mon. Wea. Rev.*, **148**, 981–1004, https://doi.org/10.1175/MWR-D-19-0185.1.

Fudeyasu, H., and Y. Wang, 2011: Balanced Contribution to the Intensification of a Tropical Cyclone Simulated in TCM4: Outer-Core Spinup Process. *J. Atmos. Sci.*, **68**, 430–449, https://doi.org/10.1175/2010JAS3523.1.

Gray, W. M., E. Ruprecht, and R. Phelps, 1975: Relative humidity in tropical weather systems. *Mon. Wea. Rev.*, **103**, 685–690, https://doi.org/10.1175/1520-0493(1975)103<0685:RHITWS>2.0.CO;2.

Guimond, S. R., P. D. Reasor, G. M. Heymsfield, and M. M. McLinden, 2020: The dynamics of vortex Rossby waves and secondary eyewall development in Hurricane Matthew (2016): New insights from radar measurements. *J. Atmos. Sci.*, **77**, 2349–2374, https://doi.org/10.1175/JAS-D-19-0284.1.

Hawkins, H. F., 1983: Hurricane Allen and Island Obstacles. *J. Atmos. Sci.*, 40, 1360–1361, https://doi.org/10.1175/1520-0469(1983)040<1360:HAAIO>2.0.CO;2.

Hawkins, J. D., M. Helveston, T. F. Lee, F. J. Turk, K. Richardson, C. Sampson, J. Kent, and R. Wade, 2006: Tropical cyclone multiple eyewall configurations. 27th Conf. on Hurricanes and Tropical Meteorology, Monterey, CA, Amer. Meteor. Soc., 6B.1.

Heng, J.-Y., Y. Wang, and W.-C. Zhou, 2017: Revisiting the balanced and unbalanced aspects of tropical cyclone intensification. *J. Atmos. Sci.*, **74**, 2575–2591. https://doi.org/10.1175/JAS-D-17-0046.1

Hong, S.-Y., Y. Noh, and J. Dudhia, 2006: A new vertical diffusion package with an explicit treatment of entrainment processes. *Mon. Wea. Rev*., **134**, 2318–2341, https://doi.org/10.1175/MWR3199.1.

Houze, R. A., Jr., S. S. Chen, B. F. Smull, W.-C. Lee, and M. M. Bell, 2007: Hurricane intensity and eyewall replacement. *Science,* **315**, 1235–1239, https://doi.org/10.1126/science.1135650.

Huang, Y.-H., M. T. Montgomery, and C.-C. Wu, 2012: Concentric eyewall formation in Typhoon Sinlaku (2008). Part II: Axisymmetric dynamical processes. *J. Atmos. Sci*., **69**, 662–674, https://doi.org/10.1175/JAS-D-11-0114.1.

Huang, Y.-H., C.-C. Wu, and M. T. Montgomery, 2018: Concentric eyewall formation in Typhoon Sinlaku (2008). Part III: Horizontal momentum budget analyses. J. Atmos. Sci., 75, 3541–3563, https://doi.org/10.1175/JAS-D-18-0037.1.

Kain, J. S., and J. M. Fritsch, 1993: Convective parameterization for mesoscale models: The Kain–Fritsch scheme. *The Representation of Cumulus Convection in Numerical Models, Meteor. Monogr*., No. 46, Amer. Meteor. Soc., 165–177.

Kepert, J. D., 2013: How does the boundary layer contribute to eyewall replacement cycles in axisymmetric tropical cyclones? *J. Atmos. Sci*., **70**, 2808–2830, https://doi.org/10.1175/JAS-D-13-046.1.

Kossin, J. P., and M. Sitkowski, 2009: An objective model for identifying secondary eyewall formation in hurricanes. *Mon. Wea. Rev*., **137**, 876–892, https://doi.org/10.1175/2008MWR2701.1.

Kossin, J. P., and Sitkowski M. , 2012: Predicting hurricane intensity and structure changes associated with eyewall replacement cycles. *Wea. Forecasting*, **27**, 484–488, https://doi.org/WAF-D-11-00106.1.

Kossin, J. P., and M. DeMaria, 2016: Reducing Operational Hurricane Intensity Forecast Errors during Eyewall Replacement Cycles. *Wea. Forecasting*, **31**, 601–608, https://doi.org/10.1175/WAF-D-15-0123.1.

Kuo, H.-C., C.-P. Chang, Y.-T. Yang, and H.-J. Jiang, 2009: Western North Pacific typhoons with concentric eyewalls. *Mon. Wea. Rev*., **137**, 3758–3770, https://doi.org/10.1175/2009MWR2850.1.

Li, Q., Y. Wang, and Y. Duan, 2014: Effects of Diabatic Heating and Cooling in the Rapid Filamentation Zone on Structure and Intensity of a Simulated Tropical Cyclone. *J. Atmos. Sci*., **71**, 3144–3163, https://doi.org/10.1175/JAS-D-13-0312.1.

Liu, X., Q. Li, and Y. Dai, 2022: Stronger vertical shear leads to earlier secondary eyewall formation in idealized numerical simulations. Geophys. Res. Lett., **49**, e2022GL098093. https://doi.org/10.1029/2022GL098093

Menelaou, K., M. K. Yau, and Y. Martinez, 2012: On the dynamics of the secondary eyewall genesis in Hurricane Wilma (2005). *Geophys. Res. Lett*., **39**, L04801, doi:10.1029/2011GL050699.

Mlawer, E. J., S. J. Taubman, P. D. Brown, M. J. Iacono, and S. A. Clough, 1997: Radiative transfer for inhomogeneous atmosphere: RRTM, a validated correlated-k model for the longwave. *J. Geophys. Res*., **102**, 16 663–16 682, https://doi.org/10.1029/97JD00237.

Montgomery, M. T., and R. T. Kallenbach, 1997: A theory for vortex Rossby-waves and its application to spiral bands and intensity changes in hurricanes. *Quart. J. Roy. Meteor. Soc*., **123**, 435–465, https://doi.org/10.1002/qj.49712353810.

Moon, Y., and D. S. Nolan, 2010: The dynamic response of the hurricane wind field to spiral rainband heating. *J. Atmos. Sci.*, **67**, 1779–1805, https://doi.org/10.1175/2010JAS3171.1.

Navarro, E. L., G. J. Hakim, and H. E. Willoughby, 2017: Balanced Response of an Axisymmetric Tropical Cyclone to Periodic Diurnal Heating. *J. Atmos. Sci*., **74**, 3325–3337, https://doi.org/10.1175/JAS-D-16-0279.1.

Noh, Y., W. G. Cheon, S. Y. Hong, and S. Raasch, 2003: Improvement of the K-profile model for the planetary boundary layer based on large eddy simulation data. *Bound.-Layer Meteor*., **107**, 401–427, https://doi.org/10.1023/A:1022146015946.

Nong, S., and K. A. Emanuel, 2003: A numerical study of the genesis of concentric eyewalls in hurricanes. Quart. *J. Roy. Meteor. Soc*., **129**, 3323–3338, https://doi.org/10.1256/qj.01.132.

Pendergrass, A. G., and H. E. Willoughby, 2009: Diabatially induced secondary flows in tropical cyclones. Part I: Quasi-steady forcing. *Mon. Wea. Rev*., **137**, 805–821, https://doi.org/10.1175/2008MWR2657.1.

Qin, N., L. Wu, and Q. Liu, 2021: Evolution of the Moat Associated with the Secondary Eyewall Formation in a Simulated Tropical Cyclone. *J. Atmos. Sci*., **78**, 4021–4035, https://doi.org/10.1175/JAS-D-20-0375.1.

Qiu, X., Z.-M. Tan, and Q. Xiao, 2010: The roles of vortex Rossby waves in hurricane secondary eyewall formation. *Mon. Wea. Rev*., **138**, 2092–2019, https://doi.org/10.1175/2010MWR3161.1.

Rozoff, C. M., D. S. Nolan, J. P. Kossin, F. Zhang, and J. Fang, 2012: The roles of an expanding wind field and inertial stability in tropical cyclone secondary eyewall formation. *J. Atmos. Sci*., **69**, 2621–2643, https://doi.org/10.1175/JAS-D-11-0326.1.

Schubert, W. H., and J. J. Hack, 1983: Transformed Eliassen balanced vortex model. *J. Atmos. Sci*., **40**, 1571–1583, https://doi.org/10.1175/1520-0469(1983)040<1571:TEBVM>2.0.CO;2.

Shapiro, L. J., and H. E. Willoughby, 1982: The response of balanced hurricanes to local sources of heat and momentum. *J. Atmos. Sci*., **39**, 378–394, https://doi.org/10.1175/1520-0469(1982)039<0378:TROBHT>2.0.CO;2.

Skamarock, W. C., J. B. Klemp, J. Dudhia, D. O. Gill, D. M. Barker, M. G. Duda, X.-Y. Huang, W. Wang, and J. G. Powers, 2008: A description of the advanced research WRF Version 3. *NCAR Tech. Note NCAR/TN-4751STR*, **113 pp**. [Available online at http://www.mmm.ucar.edu/wrf/users/docs/ arw_v3_bw.pdf.].

Sun, Y. Q., Y. Jiang, B. Tan, and F. Zhang, 2013: The governing dynamics of the secondary eyewall formation of Typhoon Sinlaku (2008). *J. Atmos. Sci*., **70**, 3818–3837, https://doi.org/10.1175/JAS-D-13-044.1.

Terwey, W. D., and M. T. Montgomery, 2008: Secondary eyewall formation in two idealized, full-physics modeled hurricanes. *J. Geophys. Res*., **113**, D12112, https://doi.org/10.1029/2007JD008897.

Tyner, B., P. Zhu, J. A. Zhang, S. Gopalakrishnan, F. Marks Jr., and V. Tallapragada, 2018: A top-down pathway to secondary eyewall formation in simulated tropical cyclones. *J. Geophys. Res*. *Atmos*., **123**, 174–197, https://doi.org/10.1002/2017JD027410.

Vigh, J. L., and W. H. Schubert, 2009: Rapid development of the tropical cyclone warm core. *J. Atmos. Sci*., **66**, 3335–3350, https://doi.org/10.1175/2009JAS3092.1.

Wang, H., C. Wu, and Y. Wang, 2016: Secondary eyewall formation in an idealized tropical cyclone simulation: Balanced and unbalanced dynamics. *J. Atmos. Sci*., **73**, 3911–3930, https://doi.org/10.1175/JAS-D-15-0146.1.

Wang, H., Y. Wang, J. Xu, and Y. Duan, 2019: The axisymmetric and asymmetric aspects of the secondary eyewall formation in a numerically simulated tropical cyclone under idealized conditions on an f plane. *J. Atmos. Sci*., **76**, 357–378, https://doi.org/10.1175/JAS-D-18-0130.1.

Wang, Y., and Z. Tan, 2020: Outer Rainbands–Driven Secondary Eyewall Formation of Tropical Cyclones. *J.*

Atmos. Sci., **77**, 2217–2236, https://doi.org/10.1175/JAS-D-19-0304.1.

Wang, Y., and Z. Tan, 2022: Essential Dynamics of the Vertical Wind Shear Affecting the Secondary Eyewall Formation in Tropical Cyclones. *J. Atmos. Sci*., **79**, 2831–2847, https://doi.org/10.1175/JAS-D-21-0340.1.

Wang, Y., 2007: A multiply nested, movable mesh, fully compressible, nonhydrostatic tropical cyclone model—TCM4: Model description and development of asymmetries without explicit asymmetric forcing. *Meteor. Atmos. Phys*., **97**, 93–116, https://doi.org/10.1007/s00703-006-0246-z.

Wang, Y., 2009: How Do Outer Spiral Rainbands Affect Tropical Cyclone Structure and Intensity?. *J. Atmos. Sci*., **66**, 1250–1273, https://doi.org/10.1175/2008JAS2737.1.

Willoughby, H. E., 1979: Excitation of Spiral Bands in Hurricanes by Interaction Between the Symmetric Mean Vortex and a Shearing Environmental Steering Current. *J. Atmos. Sci*., **36**, 1226–1235, https://doi.org/10.1175/1520-0469(1979)036<1226:EOSBIH>2.0.CO;2.

Willoughby, H. E., J. A. Clos, and M. G. Shoreibah, 1982: Concentric eye walls, secondary wind maxima, and the evolution of the hurricane vortex. *J. Atmos. Sci*., **39**, 395–411, https://doi.org/10.1175/1520-0469(1982)039<0395:CEWSWM>2.0.CO;2.

Wunsch, K. E. D., and A. C. Didlake Jr., 2018: Analyzing tropical cyclone structures during secondary eyewall formation using aircraft in situ observations. *Mon. Wea. Rev*., **146**, 3977–3993, https://doi.org/10.1175/MWR-D-18-0197.1.

Yang, Y.-T., H.-C. Kuo, E. A. Hendricks, and M. S. Peng, 2013: Structural and intensity changes of concentric eyewall typhoons in the western North Pacific basin. *Mon. Wea. Rev*., **141**, 2632–2648, https://doi.org/10.1175/MWR-D-12-00251.1.

Yu, C. L., A. C. Didlake, F. Zhang, and R. G. Nystrom, 2021: Asymmetric rainband processes leading to secondary eyewall formation in a model simulation of Hurricane Matthew (2016). *J. Atmos. Sci*., **78**, 29–49, https://doi.org/10.1175/JAS-D-20-0061.1.

Zhang, F., D. Tao, Y. Q. Sun, and J. D. Kepert, 2017: Dynamics and predictability of secondary eyewall formation in sheared tropical cyclones. *J. Adv. Model. Earth Syst*., **9**, 89–112, https://doi.org/10.1002/2016MS000729.

Zhang, G., and W. Perrie, 2018: Effects of asymmetric secondary eyewall on tropical cyclone evolution in Hurricane Ike (2008). *Geophys. Res. Lett*., **45**, 1676–1683, https://doi.org/10.1002/2017GL076988.

Zhu, X., H. Yu, and Y. Wang, 2022: Downwind Development in a Stationary Band Complex Leading to the Secondary Eyewall Formation in the Simulated Typhoon Soudelor (2015). *Mon. Wea. Rev*., **150**, 2459–2483, https://doi.org/10.1175/MWR-D-21-0318.1.

Zhu, Z., and P. Zhu, 2014: The role of outer rainband convection in governing the eyewall replacement cycle in numerical simulations of tropical cyclones. *J. Geophys. Res. Atmos*., **119**, 8049–8072, https://doi.org/10.1002/2014JD021899.